

Ray-tracing log-normal simulation for weak gravitational lensing: application to the cross-correlation with galaxies

Ryu Makiya,^a Issha Kayo,^b Eiichiro Komatsu^{c,a}

^aKavli Institute for the Physics and Mathematics of the Universe, Todai Institutes for Advanced Study, the University of Tokyo, Kashiwa, Japan 277-8583 (Kavli IPMU, WPI)

^bDepartment of Liberal Arts, Tokyo University of Technology, 5-23-22 Nishikamata, Ota-ku, Tokyo, Japan

^cMax-Planck-Institut für Astrophysik, Karl-Schwarzschild-Str. 1, 85741 Garching, Germany

E-mail: ryu.makiya@ipmu.jp, kayouissha@stf.teu.ac.jp,
komatsu@mpa-garching.mpg.de

Abstract. We present an algorithm to self-consistently generate mock weak gravitational lensing convergence fields and galaxy distributions in redshift space. We generate three-dimensional cosmic density fields that follow a log-normal distribution, and ray-trace them to produce convergence maps. As we generate the galaxy distribution from the same density fields in a manner consistent with ray-tracing, the galaxy-convergence cross-power spectrum measured from the mock agrees with the theoretical expectation with high precision. We use this simulation to forecast the quality of galaxy-shear cross-correlation measurements from the Subaru Hyper Suprime-Cam (HSC) and Prime Focus Spectrograph (PFS) surveys. We find that the nominal HSC and PFS surveys would detect the cross power spectra with signal-to-noise ratios of 20 and 5 at the lowest ($z = 0.7$) and highest ($z = 2.2$) redshift bins, respectively.

Contents

1	Introduction	1
2	Basics of the weak gravitational lensing effect	3
2.1	Shear and convergence fields	3
2.2	Angular power spectra of the convergence field	5
3	Log-normal simulation	5
3.1	Weak lensing convergence field	6
3.2	Galaxy positions in redshift space	9
3.3	Power spectrum measurement	9
4	Validation of the mocks	10
4.1	Simulation settings	10
4.2	Auto-power spectrum of the convergence field	10
4.2.1	Single source redshift	10
4.2.2	Multiple source redshifts	12
4.3	Cross spectra	13
5	Forecasting the Subaru PFS and HSC	14
6	Summary and Conclusions	17
A	Modifications to RAYTRIX	19

1 Introduction

The large-scale structure (LSS) of the universe is a powerful tool for cosmology [1]. It has been intensively studied using various probes such as galaxy clustering and weak gravitational lensing shear fields. See refs. [2–7] for recent measurements.

The galaxy clustering in redshift space, mainly measured from spectroscopic galaxy samples, offers a probe of the expansion history of the universe as well as the growth rate of the structure through the baryon acoustic oscillations [8, 9] and the redshift space distortion (RSD) [10–12]. A key ingredient in the analysis of the galaxy clustering is a galaxy bias (see [13] for a review), which relates the clustering amplitude of galaxies to the underlying dark matter density fields. The galaxy bias is usually treated as nuisance parameters, which limit the constraining power of the galaxy clustering on cosmological parameters.

The cosmological weak gravitational lensing effect is a magnification and coherent distortion of galaxy images induced by the intervening matter density field [14]. Unlike the galaxy clustering, the weak lensing effect offers a measure of the total matter density field free from the galaxy bias, since it is purely gravitational. It also allows us to study the expansion history and the growth of matter density fields. However, one of the disadvantages of the cosmological weak lensing effect is its low redshift resolution. Since the amplitude of the lensing power spectrum is determined by the line-of-sight integral of the matter density field, it is not straightforward to perform the “tomographic” analysis of the lensing data alone.

The galaxy clustering and the weak lensing effect are complimentary, as their joint analysis can lift degeneracy between the galaxy bias and the cosmological parameters. The cross-correlation of the spectroscopic galaxy samples and the weak lensing effect enables us to perform the redshift tomography of the gravitational lensing shear and convergence fields. Furthermore, the multi-probe analysis is useful for finding potential systematics in each of the LSS surveys, to obtain robust results.

There are several on-going and planned LSS surveys aiming to observe the galaxy clustering and the weak lensing effect with unprecedented precision [2–7]. In this paper we take the weak lensing survey from the Subaru Hyper-Prime Cam (HSC) [5] and the spectroscopic galaxy redshift survey from the Prime Focus Spectrograph (PFS) [15] as an example. The HSC provides precise maps of the cosmic shear field, while the PFS, a fiber-fed multi-object spectrograph, will perform a spectroscopic galaxy survey on top of the HSC photometric galaxy samples. A joint analysis of the HSC and PFS data will provide new insights for cosmology. Other planned LSS survey projects include Dark Energy Spectroscopic Instrument (DESI) [16], Legacy Survey of Space and Time (LSST) by Vera C. Rubin Observatory [17], Nancy Grace Roman Space Telescope [18] and Euclid [19].

To extract robust cosmological results from the LSS surveys, it is important to understand statistical and systematic uncertainties both in the model and observations. An end-to-end simulation is an essential tool for understanding these uncertainties. To this end, N -body simulations have often been used. For example, the authors of ref. [20] generated full-sky cosmic shear and convergence maps by ray-tracing N -body simulations of dark matter halos, and the mock HSC shear catalog generated from it has been used in the HSC cosmology analysis [21]. However, as LSS surveys become increasingly larger, the required number of simulations also increases, demanding more computational resources.

The so-called “log-normal simulation” offers a computationally less expensive alternative. While this kind of simulations do not capture physics completely correctly, they are useful for capturing basic summary statistics such as the two-point correlation function (which is provided as the input to the simulation) and the associated covariance matrix [22–28], and testing real-world issues such as the effects of a survey window function [22], interlopers [29], and fiber collisions [30] via end-to-end simulations.

In the log-normal method, matter density fields are generated to follow the desired clustering properties instead of solving the gravitational evolution from initial conditions, assuming that their probability density function (PDF) follows a log-normal distribution. This method is motivated by the observation that the one-point PDF of log-transformed density fields measured from N -body simulations is approximately a Gaussian [31–36], and the two-point PDF also follows approximately a multivariate log-normal distribution [37]. The lognormal method, by design, generates the density fluctuation field whose one-point and two-point statistics are consistent with the N -body simulations, although the direct field-to-field comparison is not possible because the lognormal simulation does not solve the evolution of density fluctuation.

There are several other ‘approximate methods’ for the gravitational structure formation [see 38, for review]. Ref. [27, 28, 39] performed a systematic comparison of the clustering measurements of those ‘approximate methods’, including the log-normal method, with a reference N -body simulation. They show that the real space two-point clustering matches with the N -body and other approximate methods, although the bispectrum and the redshift space clustering measurements of the lognormal method show deviations from the N -body simulation. They also show that the computational cost of the lognormal method is still less

expensive than others, such as the method based on the Lagrangian perturbation theory; thus it is still useful to develop the lognormal code. Another advantage of the log-normal method is that the statistical properties of the output fields are predictable from the inputs by design. This property makes it easier to test the real-world issues and systematics related to the observations (a few examples were mentioned above) without worrying about numerical uncertainties and computational costs associated with physical simulations.

In this paper we present a new code, `lognormal_lens`, which generates simulated distributions of the weak lensing convergence field and galaxies in redshift space from the common three-dimensional log-normal matter density field in a self-consistent manner. This code is based on publicly available `lognormal_galaxies` [25] and ray-tracing RAYTRIX [40] codes. We use `lognormal_galaxies` to generate matter density, velocity, and galaxy density fields from the input power spectrum, and compute galaxy power spectra in redshift space. We then construct a light cone from the matter density fields and ray-trace it using RAYTRIX to obtain a weak lensing convergence map. The `lognormal_lens` also computes auto- and cross-power spectra of the weak lensing convergence and galaxy density fields, which enables us to measure the cross-covariance of galaxy power spectra in redshift space and cosmic shear two-point functions. After validating the `lognormal_lens` code, we use it to generate mock data of the HSC and PFS and study how well they can measure the cross-correlation power spectra of weak lensing and galaxy density fields.

Our new code is complementary to the existing log-normal codes such as FLASK for weak lensing [24] and CoLoRe [23] for the 21-cm line intensity mapping. FLASK, which is used for the analysis of the Dark Energy Survey cosmic shear data, generates all-sky maps of the galaxy density and cosmic shear and convergence fields. Instead of ray-tracing the three-dimensional density fields, FLASK generates random realizations of the convergence field on a two-dimensional sphere from input angular power spectra assuming that it follows a distorted log-normal PDF. FLASK does not produce the velocity field; thus, the anisotropic galaxy power spectrum in redshift space is given as an input. CoLoRe generates mock observations of 21-cm line intensity mapping and RSD, but does not generate weak lensing shear fields.

The paper is organized as follows. In Section 2 we review basics of the weak gravitational lensing effect. In Section 3 we describe our method for generating the weak lensing convergence field. In Section 4 we validate our algorithm by comparing the simulated auto- and cross-spectra with the theoretical predictions. In Section 5 we present the forecast for the future Subaru PFS and HSC surveys. We summarize and conclude in Section 6. In Appendix A we describe the modifications to RAYTRIX.

2 Basics of the weak gravitational lensing effect

2.1 Shear and convergence fields

The weak lensing effect is described as transformation from the unlensed ($\vec{\theta}^u$) to lensed ($\vec{\theta}$) coordinates. With the so-called Born approximation, this transformation is written as

$$\vec{\theta}^u = \vec{\theta} - \vec{\nabla}\varphi, \quad (2.1)$$

where $\vec{\nabla} = \partial/\partial\vec{\theta}$ is a two-dimensional gradient in the angular axis. The lens potential φ is defined as

$$\varphi(\vec{\theta}) = \frac{2}{c^2\chi_s} \int_0^{\chi_s} d\chi \frac{\chi_s - \chi}{\chi} \Phi(\chi, \vec{\theta}), \quad (2.2)$$

where χ_s is the comoving distance to the source and Φ is the gravitational potential. The Jacobian matrix of the lensed to unlensed coordinate transformation, A , called the magnification matrix, is commonly written as

$$A = \begin{pmatrix} 1 - \kappa - \gamma_1 & -\gamma_2 \\ -\gamma_2 & 1 - \kappa + \gamma_1 \end{pmatrix}, \quad (2.3)$$

where the convergence κ and shear fields γ_1, γ_2 are defined by

$$\kappa = \frac{1}{2} \vec{\nabla}^2 \varphi, \quad \gamma_1 = \frac{1}{2} \left(\frac{\partial^2 \varphi}{\partial \theta_1^2} - \frac{\partial^2 \varphi}{\partial \theta_2^2} \right), \quad \gamma_2 = \frac{\partial^2 \varphi}{\partial \theta_1 \partial \theta_2}. \quad (2.4)$$

From eq.(2.2) and (2.4), κ is given by

$$\kappa(\vec{\theta}) = \frac{1}{c^2 \chi_s} \int_0^{\chi_s} d\chi \frac{\chi_s - \chi}{\chi} \vec{\nabla}^2 \Phi(\chi, \vec{\theta}). \quad (2.5)$$

In eq.(2.5) we can replace $\vec{\nabla}^2$ with the three-dimensional Laplacian Δ ,

$$\Delta = \frac{1}{\chi^2} \frac{\partial}{\partial \chi} \left(\chi^2 \frac{\partial}{\partial \chi} \right) + \frac{1}{\chi^2} \vec{\nabla}^2, \quad (2.6)$$

assuming that the positive and negative contributions cancel when we integrate $\partial^2/\partial\chi^2$ along the line-of-sight [e.g., 41, 42]. Combining with the Poisson equation

$$\Delta \Phi = \frac{3H_0^2 \Omega_{m0}}{2c^2} \frac{\delta}{a}, \quad (2.7)$$

we obtain

$$\kappa(\vec{\theta}) = \frac{3H_0^2 \Omega_m}{2c^2} \int_0^{\chi_s} d\chi \frac{\chi}{a(\chi)} \left(1 - \frac{\chi}{\chi_s} \right) \delta(\chi, \vec{\theta}), \quad (2.8)$$

where a is the cosmological scale factor. This equation shows that convergence κ can be interpreted as the line-of-sight integration of the density fluctuation field δ with a lensing weight function

$$W_\kappa(\chi) = \frac{3H_0^2 \Omega_m}{2c^2} \frac{\chi}{a(\chi)} \left(1 - \frac{\chi}{\chi_s} \right). \quad (2.9)$$

If we consider κ for multiple source galaxies with a redshift distribution given by $dn_{g,s}/d\chi$, the lensing weight function is replaced by

$$W_\kappa(\chi) = \frac{3H_0^2 \Omega_m}{2c^2} \int_\chi^\infty d\chi_s \frac{dn_{g,s}(\chi_s)}{d\chi} \frac{\chi}{a(\chi)} \left(1 - \frac{\chi}{\chi_s} \right), \quad (2.10)$$

and the integration range of eq.(2.8) is altered to $[0, \infty]$. Here the source distribution function is normalized to unity, i.e., $\int_0^\infty d\chi dn_{g,s}/d\chi = 1$.

In Fourier space the convergence and shear fields are expressed as

$$\tilde{\kappa}(\vec{\ell}) = -\frac{|\vec{\ell}|^2}{2} \tilde{\varphi}(\vec{\ell}), \quad \tilde{\gamma}_1(\vec{\ell}) = -\frac{\ell_1^2 - \ell_2^2}{2} \tilde{\varphi}(\vec{\ell}), \quad \tilde{\gamma}_2(\vec{\ell}) = -\ell_1 \ell_2 \tilde{\varphi}(\vec{\ell}), \quad (2.11)$$

where the tildes denote Fourier transformed quantities and $\vec{\ell} = (\ell_1, \ell_2)$ is the wave-number vector. The convergence and shear fields are related by

$$\tilde{\gamma}_1(\vec{\ell}) = \cos(2\phi_\ell) \tilde{\kappa}(\vec{\ell}), \quad \tilde{\gamma}_2(\vec{\ell}) = \sin(2\phi_\ell) \tilde{\kappa}(\vec{\ell}), \quad (2.12)$$

where ϕ_ℓ is defined as $(\cos \phi_\ell, \sin \phi_\ell) = (\ell_1/\ell, \ell_2/\ell)$. If we consider the following coordinate rotation,

$$\begin{pmatrix} \tilde{\gamma}_E \\ \tilde{\gamma}_B \end{pmatrix} = \begin{pmatrix} \cos 2\phi_\ell & \sin 2\phi_\ell \\ -\sin 2\phi_\ell & \cos 2\phi_\ell \end{pmatrix} \begin{pmatrix} \tilde{\gamma}_1 \\ \tilde{\gamma}_2 \end{pmatrix}, \quad (2.13)$$

we find

$$\tilde{\gamma}_E = \tilde{\kappa}, \quad \tilde{\gamma}_B = 0. \quad (2.14)$$

These shear components $\tilde{\gamma}_E$ and $\tilde{\gamma}_B$ are called the E - and B -mode, respectively.

2.2 Angular power spectra of the convergence field

The power spectrum (or the two-point correlation function) is the commonly-used summary statistics of the observed cosmic shear field. In the following we focus on the convergence rather than shear, since the relationship between the convergence and matter density fields is simpler, and the shear can be obtained from the convergence by eq.(2.14) if there is no ambiguity in the E - and B -mode separation.

The convergence κ is expressed as the line-of-sight integration of the matter density fluctuation δ weighted by the lensing kernel W_κ , and thus the angular power spectrum of κ is also written as the weighted line-of-sight integration of the matter power spectrum P_{mm} . With the Limber approximation [43], the angular auto-power spectrum of convergence field is written as

$$C^{\kappa\kappa}(\ell) = \int_0^\infty d\chi W_\kappa^2(\chi) \chi^{-2} P_{\text{mm}}((\ell + 0.5)/\chi, z). \quad (2.15)$$

Analogously, the cross power spectrum of the galaxy density and convergence fields $C_\ell^{\kappa g}$ and the angular auto power spectrum of galaxies C_ℓ^{gg} are written as

$$C^{\kappa g}(\ell) = \int_0^\infty d\chi W_\kappa(\chi) W_g(\chi) \chi^{-2} P_{\text{gm}}((\ell + 0.5)/\chi, z), \quad (2.16)$$

and

$$C^{gg}(\ell) = \int_0^\infty d\chi (\chi) W_g^2(\chi) \chi^{-2} P_{\text{gg}}((\ell + 0.5)/\chi, z), \quad (2.17)$$

where P_{gm} and P_{gg} are the galaxy-matter cross-power spectrum and the galaxy auto power spectrum, respectively. The galaxy kernel W_g is the radial distribution of lens galaxies normalized to unity, $dn_g/d\chi$.

3 Log-normal simulation

The `lognormal_lens` code is based on our lognormal code `lognormal_galaxies`¹, which generates a density field on regular grids from an input power spectrum, or, equivalently, two-point correlation function, assuming that the density field follows the log-normal PDF as follows.

The code first generates the log-transformed density fluctuation field $\ln[1 + \delta(\mathbf{x})]$ which follows the Gaussian random field characterized by the two-point correlation function $\xi^G(r)$. The Gaussian correlation function $\xi^G(r)$ is related to the input correlation function $\xi(r)$ as [31]

$$\xi^G(r) = \ln[1 + \xi(r)]. \quad (3.1)$$

¹The code is also publicly available at <http://wwwmpa.mpa-garching.mpg.de/~komatsu/codes.html>.

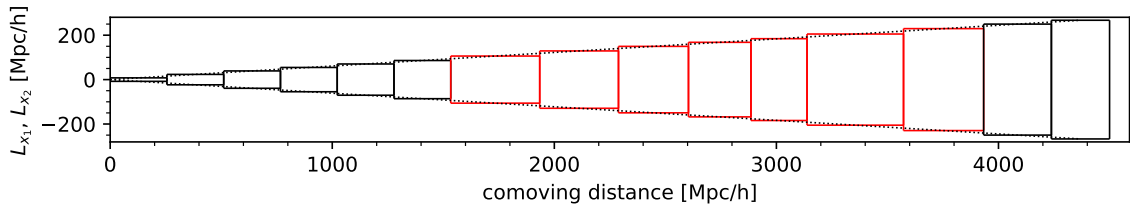


Figure 1: Configuration of the light cone with rectangular simulation boxes. The matter density field is generated in each box. The black dotted lines show the boundary of a $7 \times 7 \text{ deg}^2$ field of view. We generate galaxies in boxes with the red boundaries, mocking spectroscopic samples.

Then the density fluctuation field $\delta(\mathbf{x})$ is obtained by exponentiating the log-transformed field. Note that this treatment naturally satisfies the physical constraint on the density contrast, $\delta > -1$, which is not the case for the Gaussian random field with large variance such as of galaxies. We caution that the lognormal method is not guaranteed to reproduce the higher-order correlations of density field. Indeed, Ref.[39] shows that the `lognormal_galaxies` does not reproduce the halo bispectrum measured from the N -body simulation.

For the matter density field we use the linear matter spectrum as an input, while for the galaxy density field we use the linear galaxy power spectrum which is obtained by multiplying the linear bias squared to the matter power spectrum. We do not implement any non-linear galaxy bias into our simulations. The mock galaxies are then Poisson sampled from the underlying galaxy density field with the mean number given as inputs. We use the same random seed for the Gaussian field of galaxies and matter, to ensure that the galaxy density field and matter density field are correlated. The code also generates the peculiar velocity field of galaxies from the underlying matter density field by using the linear continuity equation.

We refer the readers to ref. [25] for further details of `lognormal_galaxies`.

3.1 Weak lensing convergence field

In `lognormal_lens` we ray-trace a light-cone of the matter density field to obtain the weak lensing convergence and shear fields. Ray-tracing is performed by the public code RAYTRIX [40]. As is done by Ref.[24], the weak lensing fields can be approximated by the distorted lognormal fields without constructing light cone. However one of our purpose is to measure the cross correlation between convergence field and galaxies, and therefore we need to construct the light cone from the matter density fields which correlate with the galaxy density field at the same redshift.

The code first generates the light cone from a series of three-dimensional matter density fields generated by the `lognormal_galaxies`, assuming that the density field does not evolve within the redshift width of the box and the different redshift boxes are not correlated. Since the lognormal method does not solve the evolution of density fields, we can not have a light cone with the smooth transition of density fields. The light cone geometry of our fiducial simulation is shown in Figure 1.

The side lengths of boxes perpendicular to the line of sight (L_{x_1} and L_{x_2} in Figure 1) are chosen to match the opening angle of the simulation (shown in the black dotted lines)

Redshift	V_{survey} [$h^3 \text{ Gpc}^{-3}$]	\bar{n}_g [$10^{-4} h^3 \text{ Mpc}^{-3}$]	bias
$0.6 < z < 0.8$	0.59	1.9	1.18
$0.8 < z < 1.0$	0.79	6.0	1.26
$1.0 < z < 1.2$	0.96	5.8	1.34
$1.2 < z < 1.4$	1.09	7.8	1.42
$1.4 < z < 1.6$	1.19	5.5	1.50
$1.6 < z < 2.0$	2.58	3.1	1.62
$2.0 < z < 2.4$	2.71	2.7	1.78

Table 1: The PFS cosmology survey parameters.

times comoving distances (the horizontal axis) to the box centers at various z . Due to the limitation of RAYTRIX, we can only deal with a square map in angle space. In this setting the boundary of simulation boxes and the survey opening angle match; thus, we do not need to worry about the window effect due to the survey geometry.

The box length along the line of sight is chosen as follows. We first create boxes in which spectroscopic galaxy samples are generated (the red boxes in Figure 1). The positions and sizes of these boxes are determined by the assumed survey strategy. In our fiducial simulation, spectroscopic galaxies are generated at $0.6 < z < 1.6$ with the redshift interval of $\Delta z = 0.2$ and at $1.6 < z < 2.4$ with $\Delta z = 0.4$, assuming the PFS survey parameters given in Table 1. The geometry of boxes located at lower and higher redshifts than the galaxy samples are chosen to have depths similar to those of the boxes of the galaxy samples. The maximum redshift z_{max} is chosen to match the assumed redshift distribution of source galaxies. Here we set $z_{\text{max}} = 3.2$ assuming the HSC survey.

We use the plane-parallel approximation to project the three-dimensional matter density field of the i -th box, δ_i , onto the two-dimensional density field δ_i^{proj} (hereafter we refer it to as “mass sheet”) as

$$\delta_i^{\text{proj}}(x_1, x_2) = \frac{1}{N_{\text{grid},y}} \sum_{y_i} \delta_i(x_1, x_2, y_i). \quad (3.2)$$

We shall denote the comoving Cartesian coordinates of the grid center as (x_1, x_2, y) with y being the line-of-sight axis. The summation is taken over all y_i , where $N_{\text{grid},y}$ is the number of grids along the line of sight. The number of grids along the x_1 and x_2 axes are set to be equal to that of the resultant angular map, which is given as the input parameter. The number of grids along the y axis is determined so that each grid cell becomes a cube. Since the matter density field is generated to satisfy the periodic boundary condition, the mass sheet is also periodic.

Next, the code calculates the two-dimensional deflection potential of the i -th mass sheet, Ψ^i , via the Poisson equation as

$$\nabla^2 \Psi^i(x_1, x_2) = \frac{3\Omega_m H_0^2}{c^2} \delta_i^{\text{proj}}(x_1, x_2). \quad (3.3)$$

The position of light ray at the source plane, θ^s , which is at θ^1 on the image plane, is deflected as

$$\theta^s = \theta^1 - \sum_{i=1}^{n-1} \frac{(\chi_s - \chi_i)}{a(\chi_i)\chi_s} \nabla_{\perp} \Psi^i, \quad (3.4)$$

where ∇_{\perp} is $\partial/\partial x_1$ or $\partial/\partial x_2$, χ_i is the comoving distance to the i -th mass sheet, and χ_s is the comoving distance to the source plane. The source plane is located at the n -th mass sheet, i.e., $\chi_s = \chi_n$.

The light ray is propagated assuming the plane-parallel approximation; thus, the spatial position of the i -th plane, \mathbf{x}^i , is converted to the angular position $\boldsymbol{\theta}^i$ as $\boldsymbol{\theta}^i = \mathbf{x}^i/\chi_i$. The code first solves eq.(3.3) using the Fast Fourier Transform, and then evaluates the derivatives of Ψ in eq.(3.4) using the finite difference method.

Along the light ray path, the Jacobian matrix of the lensed-to-unlensed coordinate transformation for sources at χ_s , A_s , is calculated as

$$A_s = I - \sum_{i=1}^{n-1} \frac{\chi_i(\chi_s - \chi_i)}{a(\chi_i)\chi_s} U_i A_i, \quad (3.5)$$

where I is the identity matrix and

$$U_i = \begin{pmatrix} \frac{\partial^2 \Psi^i}{\partial x_1 \partial x_1} & \frac{\partial^2 \Psi^i}{\partial x_1 \partial x_2} \\ \frac{\partial^2 \Psi^i}{\partial x_2 \partial x_1} & \frac{\partial^2 \Psi^i}{\partial x_2 \partial x_2} \end{pmatrix}. \quad (3.6)$$

Finally, we obtain the weak lensing convergence field, $\kappa_s(x_1, x_2)$, from $A_s(x_1, x_2)$ by using the relation of eq.(2.3). This is the convergence field for one source plane at χ_s .

The convergence map for sources with a redshift distribution of $p(z)$, κ^{tot} , is obtained by summing κ_s with a weight,

$$\kappa^{\text{tot}} = \sum_{i=i_{\min}}^{i_{\max}} w_i \kappa_i, \quad (3.7)$$

with

$$w_i = \int_{z_i - \Delta z_i/2}^{z_i + \Delta z_i/2} dz p(z). \quad (3.8)$$

Here z_i and Δz_i are the redshift and redshift interval of the i -th box, and i_{\min} and i_{\max} are the minimum and maximum redshifts of source galaxies, respectively. The redshift distribution $p(z)$ should be normalized to unity in $(z_{i_{\min}} - \Delta z_{i_{\min}}/2) < z < (z_{i_{\max}} + \Delta z_{i_{\max}}/2)$. By varying the redshift range of source galaxies (i.e., varying i_{\min} and i_{\max}), we can perform the tomographic analysis of the convergence field.

In the current cosmological weak lensing surveys, statistical errors are dominated by the shape noise from the scatter of intrinsic morphology of source galaxies. We assume that the shape noise follows a Gaussian distribution with the variance σ_N^2 given by

$$\sigma_N^2 = \frac{\sigma_{\gamma}^2}{\bar{n}_g \Omega_{\text{pix}}}, \quad (3.9)$$

where Ω_{pix} is the pixel size of the convergence map, σ_{γ} is the rms shear due to the intrinsic galaxy ellipticity and \bar{n}_g is the mean number density of source galaxies. Figure 2 shows the final lensing convergence map obtained by our `lognormal_lens` with and without shape noise. We set $\sigma_{\gamma} = 0.22$ and $\bar{n}_g = 14.6 \text{ arcmin}^{-2}$ in $0.6 < z < 3.2$, which are typical values of the HSC weak lensing survey.

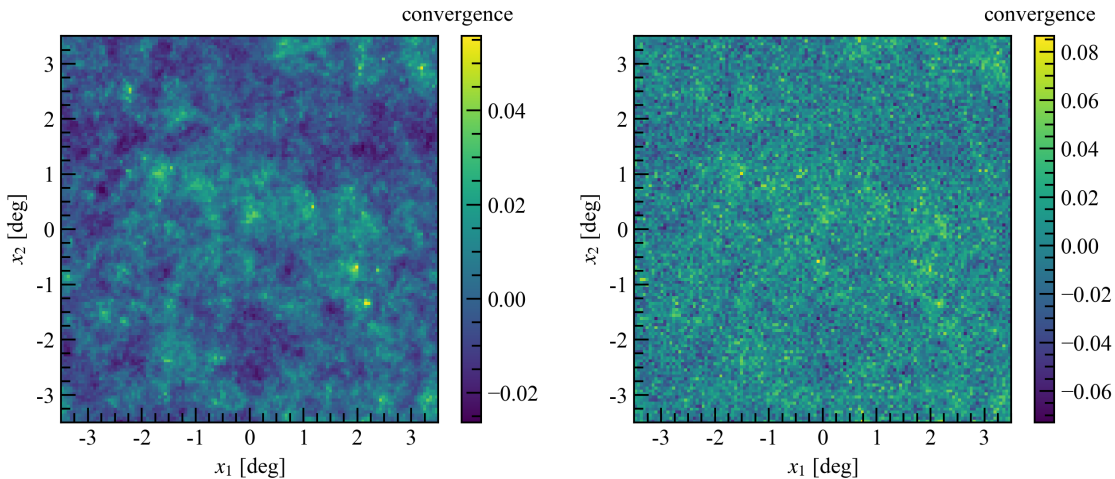


Figure 2: A mock convergence map without (left) and with (right) shape noise. The source galaxies are distributed in $0.6 < z < 3.2$. The shape noise parameters are set to be typical values of the HSC survey, $\sigma_\gamma = 0.22$ and $\bar{n}_g = 14.6 \text{ arcmin}^{-2}$.

3.2 Galaxy positions in redshift space

The `lognormal_galaxies` code generates the galaxy positions and the velocity field in addition to the matter density field. We can measure the three-dimensional power spectrum in redshift space as well as the angular power spectrum of galaxies, which should correlate with the convergence field described in the previous section.

To cross-correlate with the convergence fields, we also use the plane-parallel approximation to project the three-dimensional galaxy density field δ_{gal} onto the two-dimensional galaxy density field $\delta_{\text{gal}}^{\text{proj}}$ in the same manner as the matter density field,

$$\delta_{\text{gal}}^{\text{proj}}(x_1, x_2) = \frac{1}{N_{\text{grid},y}} \sum_{y_i} \delta_{\text{gal}}(x_1, x_2, y_i). \quad (3.10)$$

The spatial position (x_1, x_2) is converted to the angular position as $(\theta_1, \theta_2) = (x_1/\chi, x_2/\chi)$ where χ is the comoving distance to the center of the simulation box.

3.3 Power spectrum measurement

From the mock observable fields x and y , we compute the angular power spectrum as

$$\ell'^2 \mathcal{C}^{xy}(\ell') = \frac{1}{L^2} \left[\frac{1}{N_{\text{mode},b}} \sum_{\ell \in \ell_b} \ell^2 \delta^x(\ell) \delta^{y*}(\ell) \right], \quad (3.11)$$

where L is the side-length of the square-shape simulation field, ℓ_b denotes the multipole bins, $N_{\text{mode},b}$ is the number of modes within the bin, and δ^x and δ^y are the Fourier transform of the fields x and y . The bin-averaged multipole ℓ' is calculated as

$$\ell' = \frac{1}{N_{\text{mode},b}} \sum_{\ell \in \ell_b} \ell. \quad (3.12)$$

We use the logarithmically equally spaced bins with the minimum multipole of $\ell_{\min} = 2\pi/L$ and the bin width of $d \ln \ell = 0.3 \log_{10} e$. For the Fourier transformation of the fields we use the publicly available library of fast Fourier transform, FFTW [44].

4 Validation of the mocks

In this section we validate the internal consistency of our algorithm by comparing the angular auto- and cross-power spectra of the convergence and galaxy density fields from mocks with the input ones. Although it has been proved that the density field generated by `lognormal_galaxies` precisely follows the input power spectrum [25], some systematics can be introduced during the construction of the convergence fields and measurement of the power spectra. In what follows we prove that both the measured convergence auto- and convergence-galaxy cross-spectra recover the model power spectra which is calculated from the input matter and galaxy power spectra.

4.1 Simulation settings

For the fiducial simulation we use a flat Λ CDM model with the parameters of *Planck* 2015 ‘TT,TE,EE+lowP’: $\Omega_b h^2 = 0.02225$, $\Omega_c h^2 = 0.1198$, $n_s = 0.9645$, $\ln(10^{10} A_s) = 3.094$ and $h = 0.67021$ with the minimum neutrino mass of $\sum m_\nu = 0.06$ [eV] [45]. The input matter power spectra at various redshifts are calculated by the publicly available code `CLASS` [46, 47]. For simplicity, we use the linear matter power spectrum. The default field-of-view of one realization is $7 \times 7 \text{ deg}^2$ and the number of two-dimensional angular grids is $N_{\text{grid},2\text{D}} = 256$, unless otherwise noted². The square shape of the map comes from a limitation of `RAYTRIX` and we may mitigate this limit in near future. The shape noise is not included, so that we can test the simulation results precisely.

The light cone is generated in $0 < z < 3.2$ as shown in Fig. 1, consisting of 15 log-normal boxes with similar sizes along the line of sight. We confirmed that the box thickness does not significantly affect the resultant angular power spectrum.

Each log-normal box is generated with the three-dimensional grid number of $N_{\text{grid},3\text{D}} = 256$ for the axis perpendicular to the line of sight, while the grid number of the line-of-sight axis, $N_{\text{grid},y}$, is determined so that the physical size of the grid is the same with the other axis. In the redshift range covered by the PFS cosmology survey, $0.6 < z < 2.4$ (corresponding to the red boxes in Figure 1), we also generate galaxy density fields, which will be cross-correlated with the convergence field.

4.2 Auto-power spectrum of the convergence field

4.2.1 Single source redshift

First, we examine the simplest case: the convergence auto-power spectrum for a single source redshift. In this limit the lensing kernel W^κ is simplified to eq.(2.9).

The top panel of Figure 3 shows the mock and theoretical auto-power spectra of the convergence field for the source redshift of $z_s = 2.99$. The simulation data points are the mean of 2,000 realizations, while the error bars show the error of the mean for 68 percentile.

²The computational cost for a realization using one CPU core on a laptop PC is a few minutes for the default configuration.

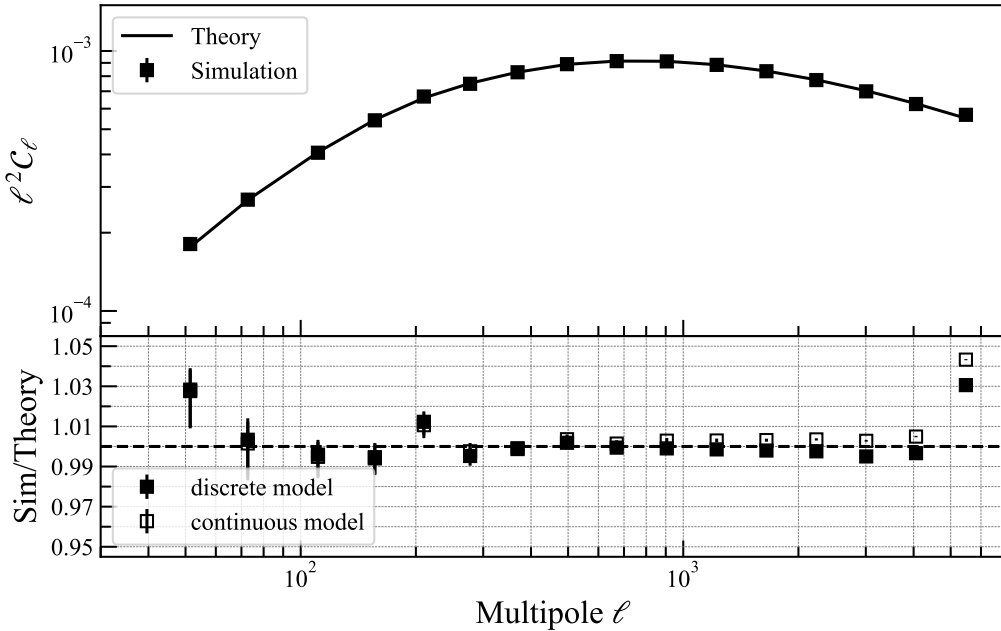


Figure 3: *Top:* Mean of 2,000 simulated angular auto power spectra of the convergence field (filled squares). The error of the mean is smaller than the size of the square. The single source plane at $z = 2.99$ is assumed. The solid line is the theoretical model with the discrete redshift integral. *Bottom:* The ratio of the simulation and the theoretical model, with (filled) and without (open) discretization of the redshift integral.

To take into account the effect of discretization in the simulation data, we evaluate the theoretical model on the same grid as in the simulations in multipole space and binned as

$$\ell'^2 \mathcal{C}^{\text{theory}}(\ell') = \frac{1}{N_{\text{mode},b}} \sum_{\ell \in \ell_b} \ell^2 \mathcal{C}^{\text{theory}}(\ell). \quad (4.1)$$

In the following we use this grid-based theoretical power spectrum when we compare the theory and mock power spectra.

Since the mock light cone is constructed from the discrete boxes, the redshift evolution of the matter density field is not smooth. To take into account this effect, we also discretize the redshift integration in the theoretical model of the convergence power spectrum, eq.(2.15), as

$$C^{\kappa\kappa}(\ell) = \sum_{i=1}^{n-1} \Delta\chi_i W_\kappa^2(\chi_i) \chi_i^{-2} P_{\text{mm}}^i((\ell + 0.5)/\chi_i), \quad (4.2)$$

where P_{mm}^i , χ_i and $\Delta\chi_i$ are the input matter power spectrum, the comoving distance and the thickness of the i -th box, respectively. The source galaxies are located at χ_n . The filled squares in the bottom panel of Figure 3 show the ratio of mock and theory obtained by the discretized model, eq.(4.2), while the open squares show that with the continuous model, eq.(2.15). The difference between two models is less than 0.5%.

The mock power spectrum matches the theoretical model with better than 1% accuracy, except the largest multipole bin in which the effect of the finite grid size of the three-dimensional matter density field is significant. This trend is also seen in the power spectrum of three-dimensional density field measured from a single lognormal box, as shown in ref. [25]. Although the lognormal method does not completely capture the real-world physics and therefore less accurate than the first principle simulations, this precise agreement between the simulation output and the input model is the main advantage of this method, as this allows us to test real-world issues without worrying about inaccuracy of the theoretical model for, e.g., N -body simulations.

The authors of ref. [20] show that one needs to take into account the effect of finite thickness of a mass sheet (called “shell” in ref. [20]), because the power in the line-of-sight direction on scales larger than the mass sheet thickness is suppressed. In our simulation, however, this effect does not appear. We generate a mass sheet at a given redshift by projecting the entire simulation box at that redshift, which satisfies the periodic boundary condition; thus, the large scale mode is not lost. On the other hand, the “shell” in ref.[20] is cut out from the simulation box larger than the shell thickness and therefore the window effect is induced.

As noted above we adopt the plane-parallel approximation when we calculate paths of light rays at the position of each mass sheet. This approximation is valid when the opening angle of the survey is sufficiently small. Although our simulation outputs would match the theoretical prediction from eq.(4.2) with arbitrary opening angles by design, such a simulation does not capture the effect of curvature of sky. We can try to incorporate the effect of sky curvature by radially propagating light rays from the observer position. We relate the angular position $\theta^i = (\theta_1, \theta_2)$ and the spatial position $\mathbf{x}^i = (x_1, x_2)$ as $(\tan \theta_1, \tan \theta_2) = (x_1/\chi_i, x_2/\chi_i)$. In this case, however, the angular grids and the spatial grids no longer match; thus, we use the cloud-in-cell (CIC) interpolation to estimate the deflection potential at arbitrary angular positions.

Figure 4 shows the ratio of the “radial ray propagation” to the “plane-parallel ray propagation” (fiducial model) results for opening angles of $7 \times 7 \text{ deg}^2$ and $3.5 \times 3.5 \text{ deg}^2$. The number of grids for the 3.5 deg simulation is 128, which is chosen to yield the same grid size as for the 7 deg simulation, i.e., both simulations have the same spatial resolution. We find that the small-scale power is suppressed in the “radial ray propagation” case. This is because the CIC interpolation smears out the small scale fluctuations. The suppression is more significant for the 7 deg simulation, because the difference in the paths of light rays between the “radial ray propagation” and “plane-parallel ray propagation” cases becomes larger at larger angles. This result shows that the projection of the density field and light-ray propagation should be done in the same way. The angular coordinate version of the RAYTRIX, GRayTrix [48, 49], can be used to perform the large opening angle simulation. Implementation of this is left for future work.

4.2.2 Multiple source redshifts

Next we investigate the convergence auto power spectrum with multiple source planes. In this case the lensing kernel W_κ is given in eq.(2.10). Since the redshift distribution of source planes is discrete in our simulation, we also discretize the redshift integral in eq.(2.10) as

$$W_\kappa(\chi_i) = \frac{3H_0^2\Omega_m}{2c^2} \sum_{j=i}^{n-1} \Delta\chi_j w_j \frac{\chi_i}{a(\chi_i)} \left(1 - \frac{\chi_i}{\chi_j}\right), \quad (4.3)$$

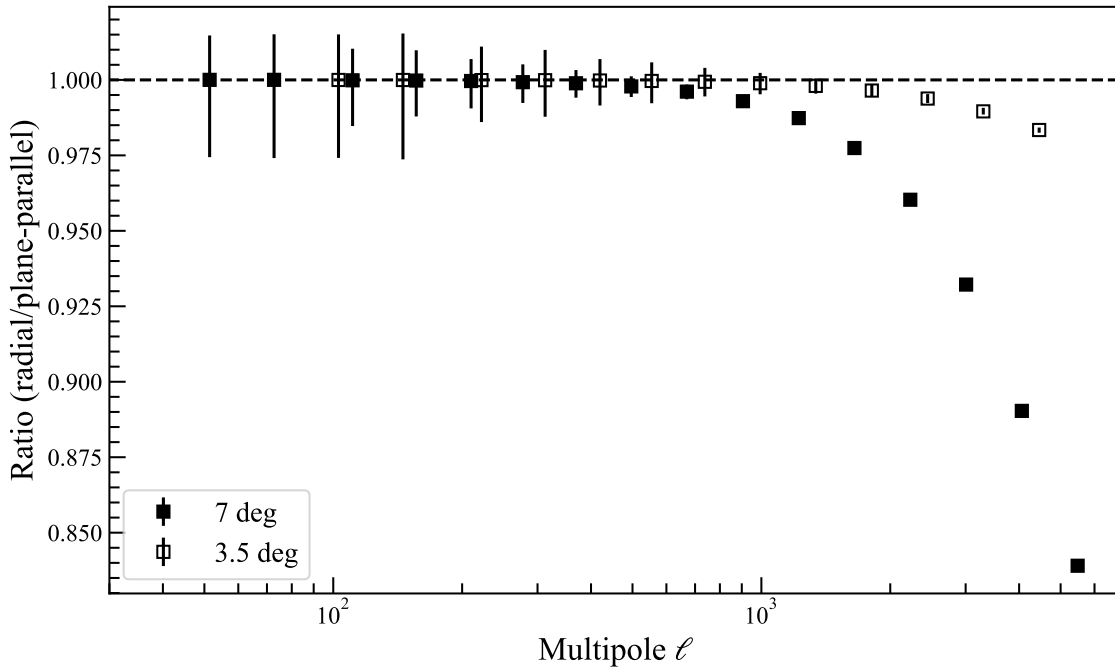


Figure 4: The ratio of the mock convergence auto-power spectra with the “radial ray propagation” and “plane-parallel ray propagation” methods. The filled squares show the results of $7 \times 7 \text{ deg}^2$ and $N_{\text{grid},2\text{D}} = 256$ simulation, while the open squares show the $3.5 \times 3.5 \text{ deg}^2$ and $N_{\text{grid},2\text{D}} = 128$ simulation.

where w_i is the weight defined in eq.(3.8). For the redshift distribution of source galaxies, $p(z)$, we assume

$$p(z) = z^2 \exp(-z/z_0), \quad (4.4)$$

with $z_0 = 1/3$, which approximates the redshift distribution of source galaxies in the HSC weak lensing survey. Figure 5 shows the convergence auto-power spectrum with source galaxies at $z > 0.6$. The mock spectrum matches the theoretical prediction at the same level as in the single source redshift case shown in Figure 3.

4.3 Cross spectra

Figure 6 and 7 show the mock galaxy-convergence cross-power spectrum for a single source plane at $z_s = 2.99$ and multiple source planes at $1.4 < z < 3.2$, respectively. The galaxies are located in the redshift slice of $1.2 < z < 1.4$, with the galaxy bias and number density set to be $b_g = 1.42$ and $n_g = 7.8 \times 10^{-2} h^3 \text{ Mpc}^{-3}$ assuming the PFS cosmology survey (Table 1) but 100 times higher number density, to suppress the shot noise. The data points are the mean of 2,000 realizations, while the error bars show the error of the mean for 68 percentile.

As with the lensing auto-power spectrum, the theoretical model of the cross spectrum defined in eq.(2.16) is also modified as

$$C^{g\kappa}(\ell) = \Delta\chi_i W_g(\chi_i) W_\kappa(\chi_i) \chi_i^{-2} P_{\text{gm}}^i((\ell + 0.5)/\chi_i), \quad (4.5)$$

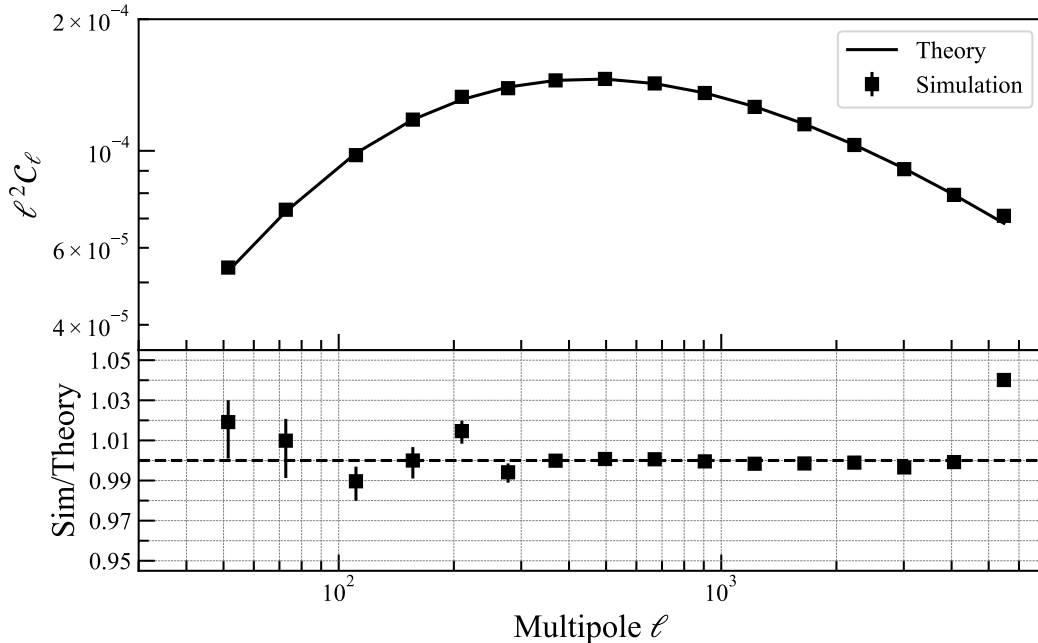


Figure 5: Same as Figure 3, but for multiple source planes at $0.6 < z < 3.2$.

where the cross correlation is taken with galaxy samples of the i -th box. The galaxy kernel W_g is the normalized redshift distribution of spectroscopic galaxy samples. Since we assume a constant number density within each box, $W_g = 1/\Delta\chi_i$. The galaxy-matter cross power spectrum P_{gm} is calculated from the input matter and galaxy power spectra following the procedure of ref. [25].

We find that the mock cross power spectra match the theoretical ones with 1% accuracy except the highest multipole, although the statistical error is large at lower multipoles. To assess potential systematics at lower multipoles, we further generate 5,000 realizations with coarser grids, $N_{\text{grid},2\text{D}} = 32$. The results are shown in the open squares in Figure 6 and 7. We find that there is no systematic deviation from the theoretical predictions at low multipoles.

As noted above, the projection of matter and galaxy density fields as well as the propagation of light rays are all done by the plane-parallel approximation. If one radially projects galaxies into a two-dimensional map, it would suppress the small-scale power due to mismatch of the galaxy positions and the underlying matter density grids. Figure 8 shows the ratio of the cross-power spectrum estimated from the radially projected galaxy map to that from the parallel projection. We find that the small scale power is significantly suppressed for the former case, showing again importance of using the same projection method for all the quantities involved.

5 Forecasting the Subaru PFS and HSC

The PFS cosmology survey will be conducted on top of the photometric galaxy catalog obtained by the HSC survey, which provides weak lensing cosmic shear maps through accurate

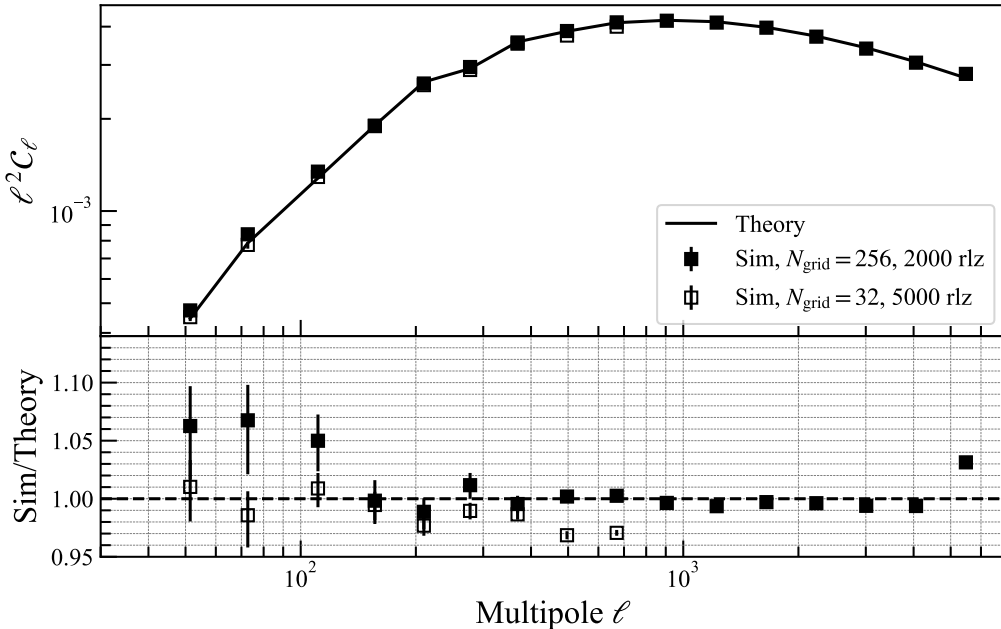


Figure 6: *Top:* Mean of 2,000 simulated galaxy-convergence cross-power spectra for galaxies in the redshift slice of $1.2 < z < 1.4$ and the single source redshift of $z_s = 2.99$ (filled squares). The error of the mean is smaller than the size of the square. The white squares show the mean of 5,000 realizations with $N_{\text{grid},2\text{D}} = 32$, to show less noisy results at small multipoles. The black solid line is the theoretical model. *Bottom:* The ratio of the simulations and the model.

measurements of galaxy shapes. The combination of the PFS and HSC data provides galaxy-shear power spectra, galaxy power spectra in redshift space, and cosmic shear power spectra over a wide range of redshifts.

We perform the `lognormal_lens` simulations for the PFS and HSC survey parameters. The survey volume, galaxy number density and galaxy bias of the PFS cosmology survey are summarized in Table 1. For the HSC survey, we assume that source galaxies have the shape noise parameter of $\sigma_\gamma = 0.22$, the number density of $n_{g,\text{source}} = 20 \text{ arcmin}^{-2}$ in $0.0 < z < 3.2$ and the redshift distribution of $p(z) = z^2 \exp(-z/z_0)$ with $z_0 = 1/3$.

The total survey area of the HSC and PFS survey is about 1400 deg^2 . To save computational costs (dominated by the high spatial resolution required for the lensing simulation), we generate 30 realizations of $7 \times 7 \text{ deg}^2$ fields with $N_{\text{grid},2\text{D}} = 128$, and average them to mock power spectra measured from the total survey area of $7 \times 7 \times 30 = 1470 \text{ deg}^2$. To measure the covariance matrix we generate 200 realizations of the mock (i.e., 6000 realizations of the $7 \times 7 \text{ deg}^2$ simulation in total).

Figure 9 shows the galaxy-convergence cross-power spectra at 7 tomographic redshift bins. We only use the source galaxies that are located at higher redshifts than the corresponding PFS galaxy samples. This figure provides a visual representation of the quality of galaxy-shear power spectra expected from the HSC and PFS surveys.

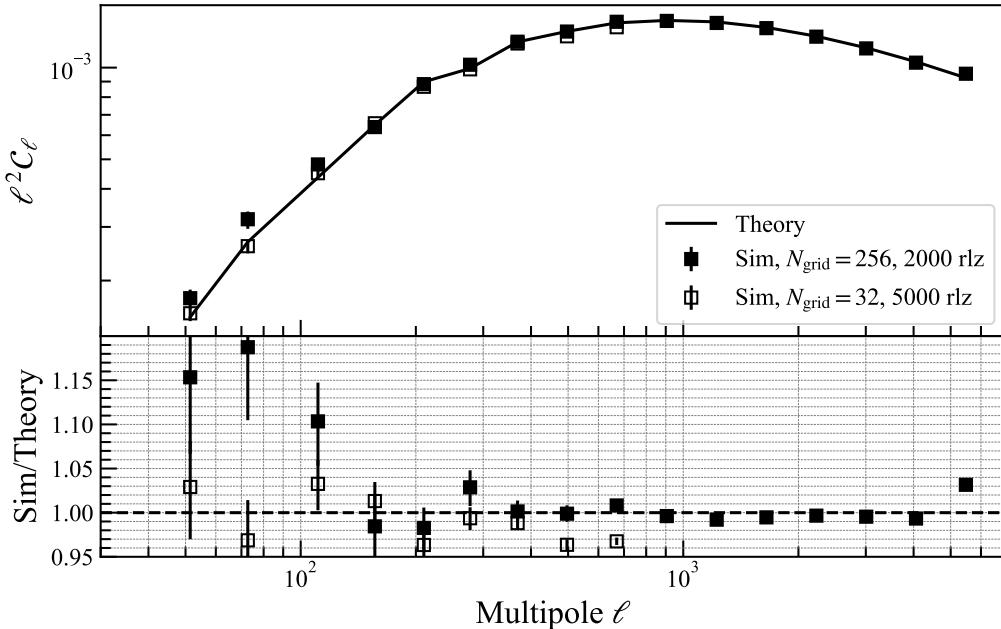


Figure 7: Same as Figure 6, but for multiple source planes at $1.4 < z < 3.2$.

Figure 10 shows the correlation coefficient matrix of the galaxy power spectrum multipoles and the galaxy-convergence cross spectra at $1.2 < z < 1.4$, estimated from 200 realizations of the mock. The range of wave numbers shown in this figure, $0.04 < k < 0.20 h/\text{Mpc}$, roughly corresponds to the multipole range of $110 < \ell < 550$ at $z = 1.3$. Our simulation results show that the covariance between the galaxy power spectrum multipoles and the galaxy-convergence cross spectrum is negligible.

We use these covariance matrices to calculate the signal-to-noise ratios of the cross spectra as

$$\left(\frac{S}{N}\right)^2 = \sum_{\ell \leq \ell'} \mathbf{C}_\ell \text{Cov}^{-1}(\ell, \ell') \mathbf{C}_{\ell'}^T. \quad (5.1)$$

We find that the PFS and HSC can measure the cross spectra with signal-to-noise ratios of 20.7, 27.6, 20.6, 18.6, 11.8, 7.6 and 5.0 at redshift bins of $z = 0.7, 0.9, 1.1, 1.3, 1.5, 1.8$ and 2.2 ($50 < \ell < 1000$), respectively. It is remarkable that secure detection of the cross power spectra is expected out to such high z , showing the power of simultaneous imaging and spectroscopy using a 8-m class telescope.

For the purpose of the validation of mock catalogs, we also calculate the signal-to-noise ratios analytically by using the following expression for the Gaussian term of the covariance matrix [50],

$$\text{Cov}^G(C_{\ell_1}^{g\kappa}, C_{\ell_2}^{g\kappa}) = \frac{\delta_{\ell_1 \ell_2}}{f_{\text{sky}}(2\ell_1 + 1)\Delta\ell_1} \left[C_{\ell_1}^{g\kappa} C_{\ell_2}^{g\kappa} + \hat{C}_{\ell_1}^{gg} \hat{C}_{\ell_2}^{\kappa\kappa} \right], \quad (5.2)$$

where δ is the Kronecker delta, $\Delta\ell$ is the multipole bin size, and $f_{\text{sky}} = 0.036$ (1470 deg^2) is the available sky fraction of the assumed survey. The galaxy and convergence auto-power spectra

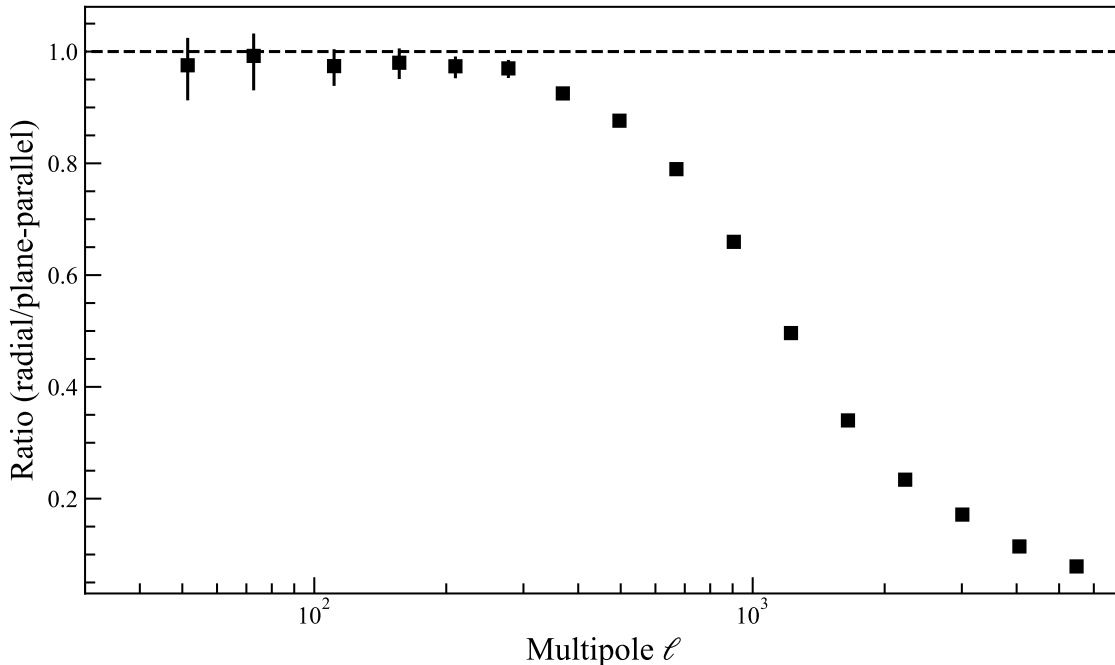


Figure 8: The ratio of the mock galaxy-convergence cross-power spectra with the “radial galaxy projection” and “plane-parallel galaxy projection” methods.

with hat symbol, $\hat{C}_{\ell_1}^{gg}$ and $\hat{C}_{\ell_2}^{\kappa\kappa}$, include the shot noise and shape noise term, respectively. They are written as

$$\hat{C}_{\ell}^{gg} = C_{\ell}^{gg} + \frac{1}{\bar{n}_{\text{g,spec}}(z)}, \quad (5.3)$$

$$\hat{C}_{\ell_2}^{\kappa\kappa} = C_{\ell}^{\kappa\kappa} + \frac{\sigma_{\gamma}^2}{\bar{n}_{\text{g,source}}(z)}, \quad (5.4)$$

where the $\bar{n}_{\text{g,spec}}(z)$ and $\bar{n}_{\text{g,lens}}(z)$ are the galaxy number density per steradian of the spectroscopic samples and source galaxies at each tomographic redshift bin, respectively. We obtain the signal-to-noise ratios of 20.8, 25.4, 19.7, 16.3, 11.4, 7.0 and 3.3 at $z = 0.7, 0.9, 1.1, 1.3, 1.5, 1.8$ and 2.2 ($50 < \ell < 1000$), which are similar to that obtained from the simulation.

6 Summary and Conclusions

We have presented the new simulation code to generate the weak lensing field based on the log-normal method of generating three-dimensional matter density, velocity and galaxy density fields. Ray-tracing the matter density fields, the code self-consistently provides the weak lensing auto power spectra, the galaxy-lensing cross-spectra and the galaxy power spectra in redshift space. The code thus offers a useful tool for generating mock observations of on-going and future LSS surveys.

The mock power spectra agree with the input model with better than 1% accuracy, which is the main advantage of the log-normal method. To achieve this precision, we found

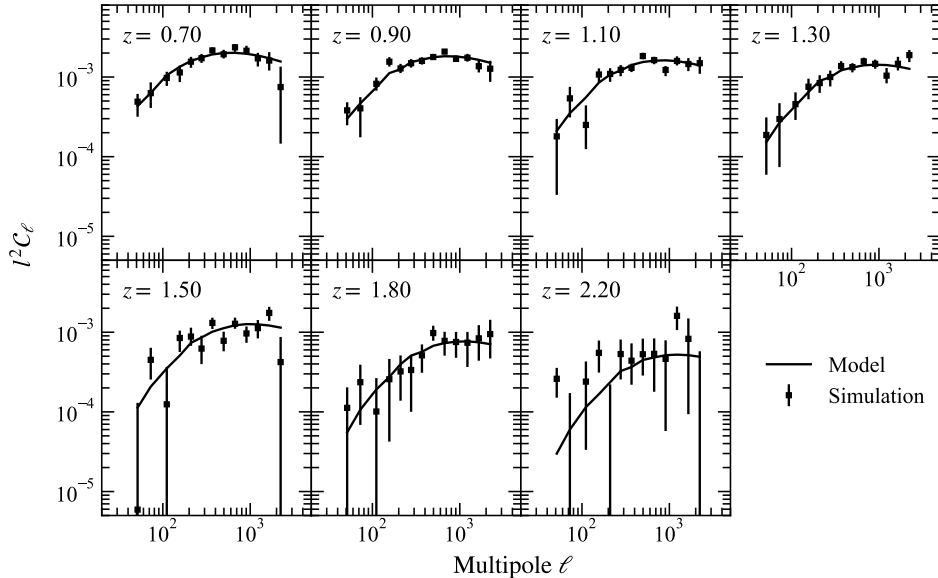


Figure 9: Galaxy-convergence cross power spectra at seven tomographic redshift bins, expected from the HSC and PFS surveys. The data points show one realization of the simulation. The error bars are the diagonal terms of the covariance matrix estimated from 200 realizations. The solid black lines show the theoretical model.

that the subtle systematics is introduced if we ignore the discreteness of simulation boxes when calculating the theoretical power spectrum. We also found that the projection of matter density and galaxy density fields and the propagation of light rays must be done in the consistent manner; otherwise, the small-scale power would be significantly suppressed.

Using this new code, we have presented forecasts for the future cosmology survey of Subaru HSC and PFS. We found that the combination of HSC and PFS data would detect the galaxy-lensing cross spectra with high signal-to-noise ratios out to unprecedentedly high redshifts. We also found that the cross-covariance between the galaxy power spectrum multipoles and the galaxy-lensing cross-spectra can be ignored at the level of statistical uncertainties of the HSC and PFS surveys.

One of the advantages of the log-normal method is that the outputs are predictable from the inputs with high accuracy, as validated in this paper. In future we use the simulation to test several systematics that arise in the real observations, e.g., the uncertainties of photometric redshift of source galaxies, non-uniform survey completeness, fiber collision, and so on.

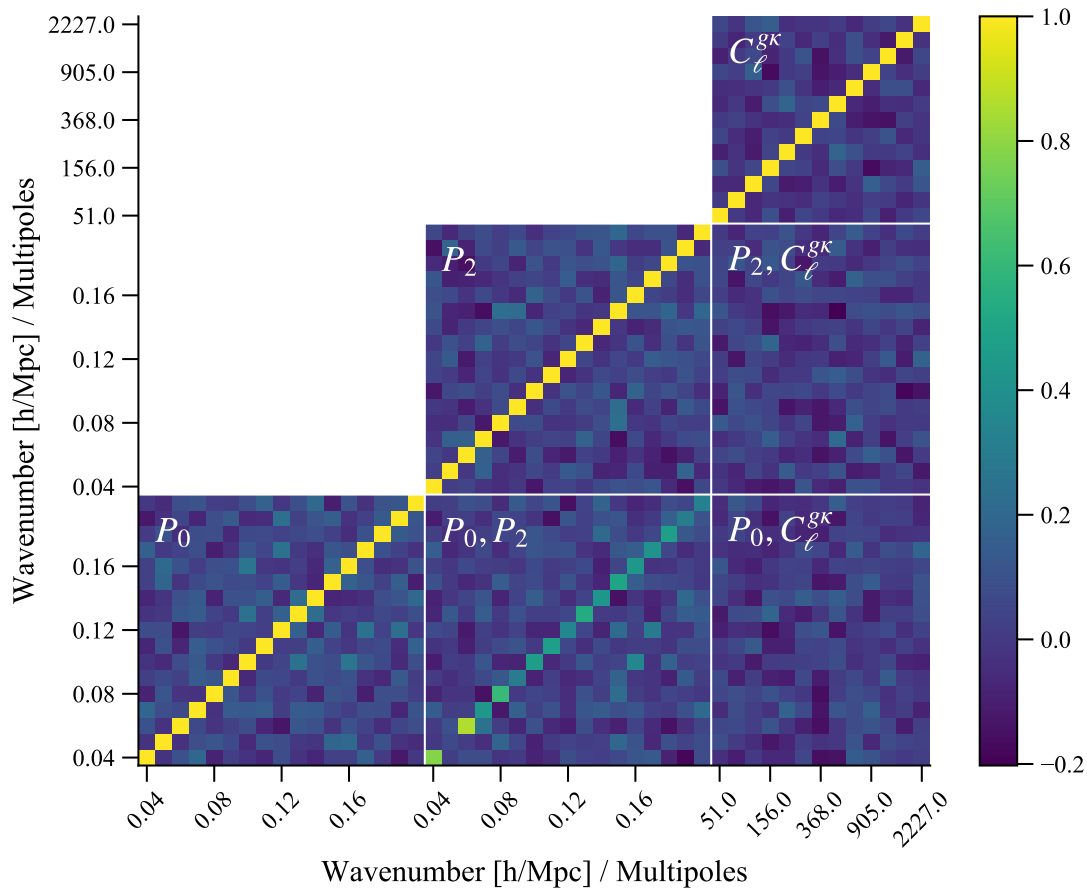


Figure 10: Correlation coefficient matrix for the galaxy power spectrum monopole (P_0), quadrupole (P_2) and the galaxy-convergence cross-power spectrum (C_ℓ^{gK}) at $1.2 < z < 1.4$ with source galaxies at $1.4 < z < 3.2$, estimated from 200 realizations of the mock.

Acknowledgments

We thank Aniket Agrawal, Aoife Boyle, Shun Saito, and Keitaro Takahashi for discussions. This work was supported in part by JSPS KAKENHI Grant Number JP15H05896 (RM, EK, IK), JP20K14515 (RM), and JP20K04016 (IK). The Kavli IPMU is supported by World Premier International Research Center Initiative (WPI), MEXT, Japan.

A Modifications to RAYTRIX

To combine with `lognormal_galaxies`, we modify RAYTRIX as follows: a) The original code requires the depth of all mass sheets to be the same (in the comoving scale). We loosen this requirement so that the code is able to handle mass sheets with various depth, because we have the PFS survey, for example, in mind, where the depth of the planned survey geometry differs between redshift ranges. b) We add a function to generate a lensing map for source galaxies with broad redshift distribution, although the original code provides maps for source galaxies on given redshifts. c) We may also add shape noise on the resulting convergence field

with the simple Gaussian distribution. We package the source codes of modified RAYTRIX into `lognormal_lens` and make it public on the internet³.

References

- [1] P. J. E. Peebles, *The large-scale structure of the universe*. Princeton University Press, 1980.
- [2] BOSS Collaboration, S. Alam, M. Ata, S. Bailey, F. Beutler, D. Bizyaev et al., *The clustering of galaxies in the completed SDSS-III Baryon Oscillation Spectroscopic Survey: cosmological analysis of the DR12 galaxy sample*, *Mon. Not. R. Astron. Soc.* **470** (Sept., 2017) 2617–2652, [[1607.03155](#)].
- [3] eBOSS Collaboration, S. Alam, M. Aubert, S. Avila, C. Balland, J. E. Bautista et al., *The Completed SDSS-IV extended Baryon Oscillation Spectroscopic Survey: Cosmological Implications from two Decades of Spectroscopic Surveys at the Apache Point observatory*, *arXiv e-prints* (July, 2020) arXiv:2007.08991, [[2007.08991](#)].
- [4] M. A. Troxel, N. MacCrann, J. Zuntz, T. F. Eifler, E. Krause, S. Dodelson et al., *Dark Energy Survey Year 1 results: Cosmological constraints from cosmic shear*, *Phys. Rev. D* **98** (Aug., 2018) 043528, [[1708.01538](#)].
- [5] C. Hikage, M. Oguri, T. Hamana, S. More, R. Mandelbaum, M. Takada et al., *Cosmology from cosmic shear power spectra with Subaru Hyper Suprime-Cam first-year data*, *Publ. Astron. Soc. Jap.* **71** (Apr., 2019) 43, [[1809.09148](#)].
- [6] H. Hildebrandt, F. Köhlinger, J. L. van den Busch, B. Joachimi, C. Heymans, A. Kannawadi et al., *KiDS+VIKING-450: Cosmic shear tomography with optical and infrared data*, *Astron. Astrophys.* **633** (Jan., 2020) A69, [[1812.06076](#)].
- [7] C. Heymans, T. Tröster, M. Asgari, C. Blake, H. Hildebrandt, B. Joachimi et al., *KiDS-1000 Cosmology: Multi-probe weak gravitational lensing and spectroscopic galaxy clustering constraints*, *arXiv e-prints* (July, 2020) arXiv:2007.15632, [[2007.15632](#)].
- [8] SDSS collaboration, D. J. Eisenstein et al., *Detection of the Baryon Acoustic Peak in the Large-Scale Correlation Function of SDSS Luminous Red Galaxies*, *Astrophys. J.* **633** (2005) 560–574, [[astro-ph/0501171](#)].
- [9] 2dFGRS collaboration, S. Cole et al., *The 2dF Galaxy Redshift Survey: Power-spectrum analysis of the final dataset and cosmological implications*, *Mon. Not. Roy. Astron. Soc.* **362** (2005) 505–534, [[astro-ph/0501174](#)].
- [10] J. C. Jackson, *A critique of Rees’s theory of primordial gravitational radiation*, *Mon. Not. R. Astron. Soc.* **156** (Jan., 1972) 1P, [[0810.3908](#)].
- [11] W. L. W. Sargent and E. L. Turner, *A statistical method for determining the cosmological density parameter from the redshifts of a complete sample of galaxies.*, *Astrophys. J. Lett.* **212** (Feb., 1977) L3–L7.
- [12] N. Kaiser, *Clustering in real space and in redshift space*, *Mon. Not. Roy. Astron. Soc.* **227** (1987) 1–27.
- [13] V. Desjacques, D. Jeong and F. Schmidt, *Large-scale galaxy bias*, *Phys. Rept.* **733** (Feb., 2018) 1–193, [[1611.09787](#)].
- [14] P. Schneider, J. Ehlers and E. E. Falco, *Gravitational Lenses*. Berlin: Springer, Verlag, 1992, [10.1007/978-3-662-03758-4](#).
- [15] PFS TEAM collaboration, M. Takada et al., *Extragalactic science, cosmology, and Galactic archaeology with the Subaru Prime Focus Spectrograph*, *Publ. Astron. Soc. Jap.* **66** (2014) R1, [[1206.0737](#)].

³See <http://wwwmpa.mpa-garching.mpg.de/~komatsu/codes.html>

- [16] M. Levi, C. Bebek, T. Beers, R. Blum, R. Cahn, D. Eisenstein et al., *The DESI Experiment, a whitepaper for Snowmass 2013*, *arXiv e-prints* (Aug., 2013) arXiv:1308.0847, [[1308.0847](#)].
- [17] Ž. Ivezić, S. M. Kahn, J. A. Tyson, B. Abel, E. Acosta, R. Allsman et al., *LSST: From Science Drivers to Reference Design and Anticipated Data Products*, *Astrophys. J.* **873** (Mar., 2019) [111](#), [[0805.2366](#)].
- [18] D. Spergel, N. Gehrels, C. Baltay, D. Bennett, J. Breckinridge, M. Donahue et al., *Wide-Field Infrared Survey Telescope-Astrophysics Focused Telescope Assets WFIRST-AFTA 2015 Report*, *arXiv e-prints* (Mar., 2015) arXiv:1503.03757, [[1503.03757](#)].
- [19] R. Laureijs, J. Amiaux, S. Arduini, J. L. Auguères, J. Brinchmann, R. Cole et al., *Euclid Definition Study Report*, *arXiv e-prints* (Oct., 2011) arXiv:1110.3193, [[1110.3193](#)].
- [20] R. Takahashi, T. Hamana, M. Shirasaki, T. Namikawa, T. Nishimichi, K. Osato et al., *Full-sky Gravitational Lensing Simulation for Large-area Galaxy Surveys and Cosmic Microwave Background Experiments*, *Astrophys. J.* **850** (Nov., 2017) [24](#), [[1706.01472](#)].
- [21] T. Hamana, M. Shirasaki, S. Miyazaki, C. Hikage, M. Oguri, S. More et al., *Cosmological constraints from cosmic shear two-point correlation functions with HSC survey first-year data*, *Publ. Astron. Soc. Jap.* **72** (Feb., 2020) [16](#), [[1906.06041](#)].
- [22] C.-T. Chiang et al., *Galaxy redshift surveys with sparse sampling*, *JCAP* **12** (2013) [030](#), [[1306.4157](#)].
- [23] D. Alonso, P. G. Ferreira and M. G. Santos, *Fast simulations for intensity mapping experiments*, *Mon. Not. Roy. Astron. Soc.* **444** (2014) [3183–3197](#), [[1405.1751](#)].
- [24] H. S. Xavier, F. B. Abdalla and B. Joachimi, *Improving lognormal models for cosmological fields*, *Mon. Not. Roy. Astron. Soc.* **459** (2016) [3693–3710](#), [[1602.08503](#)].
- [25] A. Agrawal, R. Makiya, C.-T. Chiang, D. Jeong, S. Saito and E. Komatsu, *Generating Log-normal Mock Catalog of Galaxies in Redshift Space*, *JCAP* **1710** (2017) [003](#), [[1706.09195](#)].
- [26] N. Hand, Y. Feng, F. Beutler, Y. Li, C. Modi, U. Seljak et al., *nbodykit: an open-source, massively parallel toolkit for large-scale structure*, *Astron. J.* **156** (2018) [160](#), [[1712.05834](#)].
- [27] L. Blot et al., *Comparing approximate methods for mock catalogues and covariance matrices II: Power spectrum multipoles*, *Mon. Not. Roy. Astron. Soc.* **485** (2019) [2806–2824](#), [[1806.09497](#)].
- [28] M. Lippich et al., *Comparing approximate methods for mock catalogues and covariance matrices – I. Correlation function*, *Mon. Not. Roy. Astron. Soc.* **482** (2019) [1786–1806](#), [[1806.09477](#)].
- [29] G. Addison, C. Bennett, D. Jeong, E. Komatsu and J. Weiland, *The Impact of Line Misidentification on Cosmological Constraints from Euclid and other Spectroscopic Galaxy Surveys*, *Astrophys. J.* **879** (2019) [15](#), [[1811.10668](#)].
- [30] T. Sunayama, M. Takada, M. Reinecke, R. Makiya, T. Nishimichi, E. Komatsu et al., *Mitigating the impact of fiber assignment on clustering measurements from deep galaxy redshift surveys*, *JCAP* **06** (2020) [057](#), [[1912.06583](#)].
- [31] P. Coles and B. Jones, *A lognormal model for the cosmological mass distribution.*, *Mon. Not. R. Astron. Soc.* **248** (Jan., 1991) [1–13](#).
- [32] S. Colombi, *A “skewed” lognormal approximation to the probability distribution function of the large-scale density field.*, *Astrophys. J.* **435** (Nov., 1994) [536–539](#), [[astro-ph/9402071](#)].
- [33] L. Kofman, E. Bertschinger, J. M. Gelb, A. Nusser and A. Dekel, *Evolution of One-Point Distributions from Gaussian Initial Fluctuations*, *Astrophys. J.* **420** (Jan., 1994) [44](#), [[astro-ph/9311028](#)].
- [34] F. Bernardeau and L. Kofman, *Properties of the Cosmological Density Distribution Function*, *Astrophys. J.* **443** (Apr., 1995) [479](#), [[astro-ph/9403028](#)].

- [35] C. Uhlemann, S. Codis, C. Pichon, F. Bernardeau and P. Reimberg, *Back in the saddle: large-deviation statistics of the cosmic log-density field*, *Mon. Not. R. Astron. Soc.* **460** (Aug., 2016) 1529–1541, [[1512.05793](#)].
- [36] J. Shin, J. Kim, C. Pichon, D. Jeong and C. Park, *New Fitting Formula for Cosmic Nonlinear Density Distribution*, *Astrophys. J.* **843** (July, 2017) 73, [[1705.06863](#)].
- [37] I. Kayo, A. Taruya and Y. Suto, *Probability Distribution Function of Cosmological Density Fluctuations from a Gaussian Initial Condition: Comparison of One-Point and Two-Point Lognormal Model Predictions with N-Body Simulations*, *Astrophys. J.* **561** (Nov., 2001) 22–34, [[astro-ph/0105218](#)].
- [38] P. Monaco, *Approximate methods for the generation of dark matter halo catalogs in the age of precision cosmology*, *Galaxies* **4** (2016) 53, [[1605.07752](#)].
- [39] M. Colavincenzo et al., *Comparing approximate methods for mock catalogues and covariance matrices – III: bispectrum*, *Mon. Not. Roy. Astron. Soc.* **482** (2019) 4883–4905, [[1806.09499](#)].
- [40] T. Hamana and Y. Mellier, *Numerical study of statistical properties of the lensing excursion angles*, *Mon. Not. Roy. Astron. Soc.* **327** (2001) 169, [[astro-ph/0101333](#)].
- [41] M. Bartelmann and P. Schneider, *Weak gravitational lensing*, *Phys. Rept.* **340** (2001) 291–472, [[astro-ph/9912508](#)].
- [42] M. Kilbinger, *Cosmology with cosmic shear observations: a review*, *Reports on Progress in Physics* **78** (Jul, 2015) 086901, [[1411.0115](#)].
- [43] M. LoVerde and N. Afshordi, *Extended Limber Approximation*, *Phys. Rev. D* **78** (2008) 123506, [[0809.5112](#)].
- [44] M. Frigo and S. G. Johnson, *The design and implementation of FFTW3*, *Proceedings of the IEEE* **93** (2005) 216–231.
- [45] PLANCK collaboration, P. A. R. Ade et al., *Planck 2015 results. XIII. Cosmological parameters*, *Astron. Astrophys.* **594** (2016) A13, [[1502.01589](#)].
- [46] J. Lesgourgues, *The Cosmic Linear Anisotropy Solving System (CLASS) I: Overview*, [[1104.2932](#)].
- [47] D. Blas, J. Lesgourgues and T. Tram, *The Cosmic Linear Anisotropy Solving System (CLASS) II: Approximation schemes*, *JCAP* **1107** (2011) 034, [[1104.2933](#)].
- [48] M. Shirasaki, T. Hamana and N. Yoshida, *Probing cosmology with weak lensing selected clusters - I. Halo approach and all-sky simulations*, *Mon. Not. R. Astron. Soc.* **453** (Nov., 2015) 3043–3067, [[1504.05672](#)].
- [49] T. Hamana, J. Sakurai, M. Koike and L. Miller, *Cosmological constraints from Subaru weak lensing cluster counts*, *Publ. Astron. Soc. Jap.* **67** (June, 2015) 34, [[1503.01851](#)].
- [50] W. Hu and B. Jain, *Joint galaxy - lensing observables and the dark energy*, *Phys. Rev. D* **70** (2004) 043009, [[astro-ph/0312395](#)].